Origin of Superconductivity and Latent Charge Density Wave in NbS_2

Christoph Heil,[1] Samuel Poncé,[1] Henry Lambert,[1,*] Martin Schlipf,[1] Elena R. Margine,[2] and Feliciano Giustino[1,†]
[1]Department of Materials, University of Oxford, Parks Road, Oxford OX1 3PH, United Kingdom
[2]Department of Physics, Applied Physics and Astronomy, Binghamton University-SUNY, Binghamton, New York 13902, USA
(Received 14 October 2016; revised manuscript received 19 January 2017; published 24 August 2017)

We elucidate the origin of the phonon-mediated superconductivity in $2H$-NbS_2 using the *ab initio* anisotropic Migdal-Eliashberg theory including Coulomb interactions. We demonstrate that superconductivity is associated with Fermi surface hot spots exhibiting an unusually strong electron-phonon interaction. The electron-lattice coupling is dominated by low-energy anharmonic phonons, which place the system on the verge of a charge density wave instability. We also provide definitive evidence for two-gap superconductivity in $2H$-NbS_2, and show that the low- and high-energy peaks observed in tunneling spectra correspond to the Γ- and K-centered Fermi surface pockets, respectively. The present findings call for further efforts to determine whether our proposed mechanism underpins superconductivity in the whole family of metallic transition metal dichalcogenides.

DOI: 10.1103/PhysRevLett.119.087003

Transition metal dichalcogenides (TMDs) have generated considerable interest in recent years, since they provide an ideal playground for studying semiconductors, metals, and superconductors in two dimensions using the same structural template [1–3]. In the case of superconducting TMDs, one remarkable feature is that Cooper pair condensation usually coexists with a charge density wave (CDW) [4], raising the question on whether superconductivity and the CDW cooperate or compete in these compounds [5–12].

Within the family of superconducting TMDs, $2H$-NbS_2 stands out as the only system for which a CDW phase has not been observed [13,14]. This suggests that a comparative analysis of NbS_2 and other superconducting TMDs may help to clarify the interplay between the superconductive and the CDW instabilities in the entire family. $2H$-NbS_2 is a phonon-mediated superconductor with a critical temperature $T_c = 5.7$ K. Scanning tunneling spectroscopy measurements on this compound revealed two pronounced features in the density of states (DOS) at 0.53 and 0.97 meV below the critical temperature, providing strong indications of two-gap superconductivity [14]. However, so far microscopic calculations have considered only a single-gap scenario [15,16].

In this work we investigate the nature of the superconducting gap and the pairing mechanism in $2H$-NbS_2 using the fully anisotropic *ab initio* Migdal-Eliashberg theory, and describe both electron-phonon and electron-electron interactions without any adjustable parameters. Our key finding is that a very significant contribution to the superconducting pairing comes from the low-energy anharmonic phonons with wave vectors near the line connecting the M and L points. These are the same phonons responsible for the CDW instability in other TMDs [8,11,17–19], indicating that superconductivity in NbS_2 is intimately connected with a latent CDW. In agreement with the scanning tunneling spectroscopy experiments of Ref. [14], we find two distinct and anisotropic superconducting gaps.

All calculations reported in this work were performed using density functional theory (DFT) in the local density approximation [20,21]. We employed the QUANTUM ESPRESSO package [22] for the electronic structure and lattice dynamics, the EPW code [23–25] for the electron-phonon interaction (EPI) and the superconducting gap, the STERNHEIMERGW code [26,27] for the Coulomb interaction and for GW quasiparticle calculations of the band structure, and the WANNIER90 code [28] for generating maximally localized Wannier functions [29].

$2H$-NbS_2 crystallizes in a layered hexagonal structure (space group $P6_3/mmc$), with the unit cell containing two S-Nb-S sandwiches [31]. Figure 1 shows that the Fermi surface (FS) of $2H$-NbS_2 consists of three distinct sheets: (i) a disk-shaped hole pocket centered at Γ (S_{Γ_1}), of predominant S p_z character, (ii) a cylindrical hole pocket also centered at Γ (S_{Γ_2}), arising from Nb d_{z^2} orbitals, and (iii) a triangular hole pocket centered around K (S_K) that originates from Nb-d_{z^2} states near the M point, and from d_{xy} and $d_{x^2-y^2}$ states near K.

In order to calculate the superconducting gap and critical temperature of $2H$-NbS_2, we start from the screened Coulomb interaction. Coulomb effects are included in the Migdal-Eliashberg equations via the Morel-Anderson pseudopotential $\mu^* = \mu/[1+\mu\log(\omega_{\rm el}/\omega_{\rm ph})]$ [32]. In this expression $\omega_{\rm el}$ and $\omega_{\rm ph}$ are characteristic electron and phonon energies, respectively [33], and μ is a double Fermi-surface average of the screened Coulomb interaction W: $\mu = N_F\langle\langle \mathbf{k}, -\mathbf{k}|W|\mathbf{k}', -\mathbf{k}'\rangle\rangle_{\rm FS}$, where N_F is the DOS at the Fermi level and W is calculated within the random phase approximation [26,27,36,37]. Our calculations yield

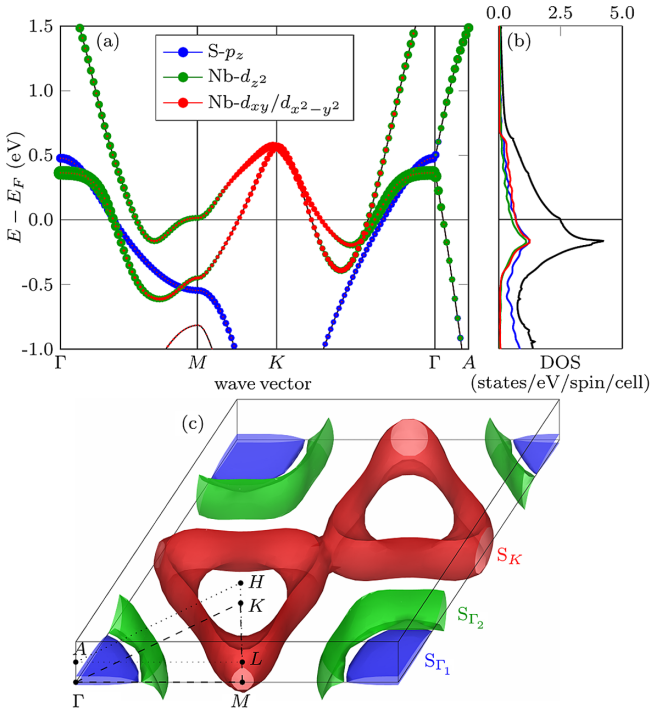

FIG. 1. (a) Calculated band structure of $2H$-NbS_2, with the orbital contributions proportional to the size of the colored dots, as indicated in the legend: S p_z (blue), Nb d_{z^2} (green), and Nb $d_{xy}/d_{x^2-y^2}$ (red). (b) Corresponding DOS and decomposition into atomic orbitals, using the same color code as in (a). The black line is the total DOS. (c) Fermi surface showing the three distinct Fermi surface sheets labeled as S_{Γ_1} (blue), S_{Γ_2} (green), and S_K (red), as well as the high-symmetry points in the Brillouin zone.

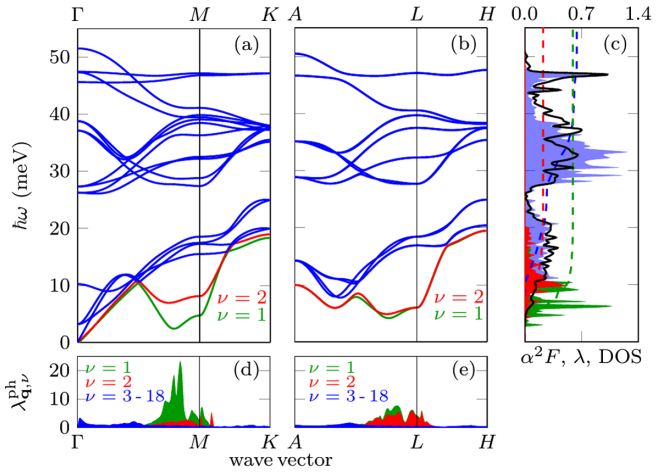

FIG. 2. (a),(b) Calculated phonon dispersion relations of $2H$-NbS_2 for the first mode ($\nu = 1$, green), the second mode ($\nu = 2$, red), and modes $\nu = 3$–18 (blue). (c) Calculated vibrational DOS (solid, black line), isotropic Eliashberg function $\alpha^2F(\omega)$ (shaded areas), and cumulative EPI strength $\lambda(\omega)$ (dashed lines). The blue curves are for modes 3–18, and the green and red curves are for the two lowest-energy phonons. (d), (e) The mode-resolved EPI strength $\lambda^{ph}_{\mathbf{q},\nu}$ for the phonon modes in (a) and (b).

$\mu^* = 0.20$ ($\mu = 0.37$), which is larger than typical values found in isotropic superconductors. This large Morel-Anderson pseudopotential originates from very strong repulsive interactions at a few Fermi surface hot spots. The electron-electron repulsion is weakest for the states corresponding to in-plane orbitals, that is, in the center of the Fermi surface sheet S_K [see Fig. 1(c) and Fig. S1 in the Supplemental Material [38]].

Figures 2(a) and 2(b) show the calculated phonon dispersion relations of $2H$-NbS_2. In the harmonic approximation the two lowest-energy vibrational modes near the M and L points of the Brillouin zone have imaginary frequencies, as shown in Figs. S2(f) and S2(g) of the Supplemental Material [38]. For each of these modes we performed fully anharmonic calculations by mapping the DFT potential energy surface, and used the renormalized anharmonic frequencies in all calculations of phonon dispersions and EPIs. The resulting dispersion relations are in good agreement with inelastic x-ray scattering experiments [19]. At the M point the anharmonic modes have A_g and B_u symmetry, respectively. The DFT potential energy surfaces of these modes correspond to symmetric double wells, and can be identified with the modes that drive the CDW instability in related TMDs [8,11,17,18]. Details about these calculations and comparisons with other methods [39–45] are provided in the Supplemental Material [38].

In Figs. 2(d) and 2(e) we show the wave vector–and mode-resolved electron-phonon coupling strength $\lambda^{ph}_{\mathbf{q},\nu}$ along high-symmetry lines. We see that the two anharmonic branches exhibit anomalously large EPIs (up to $\lambda^{ph}_{\mathbf{q},\nu=1} = 23.5$). In order to check the weight of these modes on the total EPI, we show in Fig. 2(c) the isotropic Eliashberg function $\alpha^2F(\omega)$ [25] separated into contributions arising from the two low-energy anharmonic modes (green and red), and the remaining modes (blue). The corresponding breakdown of the total EPI strength [$\lambda = 2\int_0^\infty \alpha^2F(\omega)/\omega d\omega$] is shown by the dashed lines; this analysis indicates that the anharmonic modes contribute more than 50% of the total interaction strength. At variance with these modes, the contributions of all other modes are relatively homogeneous and follow the vibrational DOS [Fig. 2(c)].

Anomalous EPI strengths of selected phonons can arise either from Fermi surface nesting effects [46], or from the breaking of electronic degeneracies by lattice fluctuations and the consequent removal of electronic weight from the DOS close to the Fermi level [47], in analogy with the dynamical Jahn-Teller effect in molecules [48]. To determine which mechanism is active in the case of $2H$-NbS_2, we calculated the Fermi surface nesting function [25,49]. By inspecting this function in Fig. S3 of the Supplemental Material [38] we see that there are no obvious nesting vectors in this system, likely because the sides of the

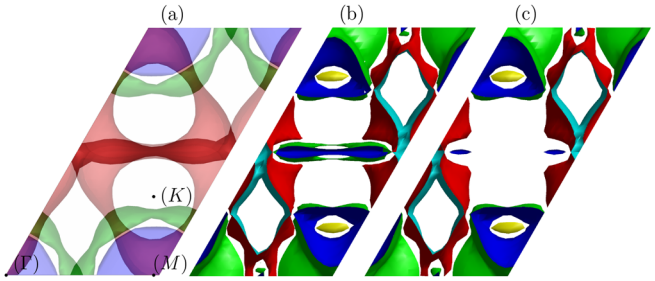

FIG. 3. (a) Sketch of the folded FS of the $2 \times 1 \times 1$ supercell, obtained by overlaying two FSs of the crystal unit cell. The high-symmetry points are indicated in brackets since they refer to the crystal Brillouin zone. (b) Calculated FS of the $2 \times 1 \times 1$ supercell in the ground-state structure. (c) Calculated FS of the $2 \times 1 \times 1$ supercell after displacing the atoms according to the B_u phonon mode at M, so as to place the structure in one of the minima of the double-well potential.

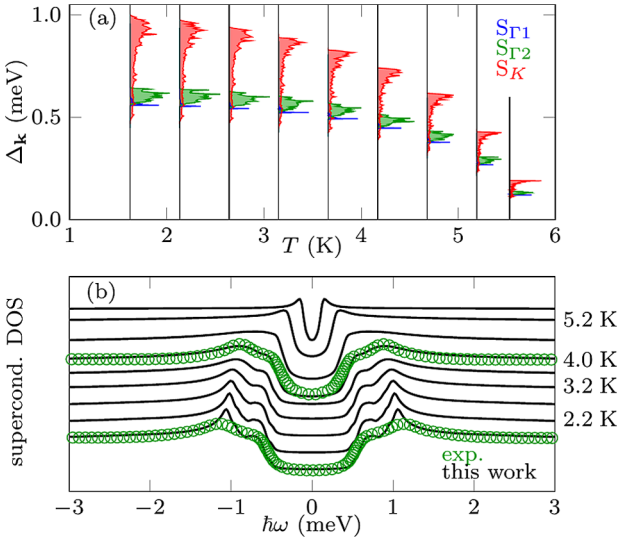

FIG. 4. (a) Energy distribution of the superconducting gap $\Delta_{\mathbf{k}}$ of $2H$-NbS_2 as a function of temperature, calculated within the anisotropic *ab initio* Migdal-Eliashberg theory including Coulomb interactions. The colors indicate data belonging to different Fermi surface sheets. (b) Calculated DOS in the superconducting phase of $2H$-NbS_2 (black lines), compared with tunneling data from Ref. [14] (green circles), for $T = 1.8$ K and $T = 4.0$ K. In both panels, to facilitate comparison with experiment, the theoretical temperature and gaps were scaled by the factors 5.7/18.6 and 0.97/4.2, respectively.

triangular Fermi pocket S_K are bulging inwards (Fig. 1). Therefore, we rule out nesting as a possible cause of strong EPIs in the anharmonic modes. This is in line with previous reports on other TMDs [7–9,50]. In order to test the second mechanism, we focused on the B_u mode at the M point. We doubled the NbS_2 unit cell along the ΓM direction so as to fold M into Γ, and calculated band structures, DOSs, and Fermi surfaces with or without a frozen B_u phonon [51]. This phonon induces avoided crossings near the Fermi level in regions that correspond to the centers of the triangular Fermi arcs S_K in Fig. 1(c). The deformation of the band structure is accompanied by a suppression of large parts of the Fermi surface in the supercell (as shown in Fig. 3 and Fig. S4 of the Supplemental Material [38]) and leads to the removal of the pronounced shoulder in the DOS close to the Fermi energy of the undistorted structure (see Fig. 1 and Fig. S5 of the Supplemental Material [38]). As pointed out in Refs. [47,52], such changes in the electronic structure are indicative of a phonon softening and a latent lattice instability, and are in line with our findings of Fermi-surface EPI hot spots precisely in the middle of the triangular sides of S_K.

We now move to the superconducting properties of $2H$-NbS_2. Figure 4(a) shows the distribution of temperature-dependent superconducting gaps on the Fermi surface, as calculated using the anisotropic *ab initio* Migdal-Eliashberg theory. Our calculations using the DFT band structure yield a critical temperature $T_c = 18.6$ K and a maximum zero-temperature superconducting gap $\Delta = 4.2$ meV, overestimating the experimental values of 5.7 K and 0.97 meV, respectively [14]. The origin of this discrepancy will be discussed below; for now, in order to facilitate comparison with experiment, we apply the empirical scaling factors 5.7/18.6 and 0.97/4.2, respectively.

The superconducting gaps in Fig. 4(a) are seen to follow the standard BCS-type temperature dependence. At each temperature the gaps cluster around two distinct values, indicating that $2H$-NbS_2 is a two-gap superconductor. The smaller gap is associated with the Fermi sheets S_{Γ_1} and S_{Γ_2}, while the larger gap belongs to S_K. From the gaps we calculate the superconducting DOS, and in Fig. 4(b) we compare our results to the tunneling experiments of Ref. [14]. The agreement between our calculations and experiments is very good (apart from the empirical scaling discussed above), and confirms that the peak around 1.0 meV and the shoulder around 0.6 meV in the tunneling data taken at 1.8 K are to be associated with two distinct superconducting gaps on the Γ-centered and on the K-centered Fermi surface pockets. Our finding of two distinct superconducting gaps is also in line with the anomalous temperature dependence of the specific heat [53] and the pressure dependence of the upper critical field [54].

Figure 5(a) shows the momentum-resolved superconducting gap on the Fermi surface. We observe finite values for $\Delta_{\mathbf{k}}$ on the whole FS; therefore, the FS is fully gapped below the critical temperature. The gaps on the S_{Γ_1} and S_{Γ_2} sheets exhibit narrow distributions centered around 0.57 meV and 0.56–0.65 meV, respectively. In contrast, the gap on the S_K sheet is highly anisotropic and varies over the wide range 0.5–1.0 meV [Fig. 5(b)]. By recalling the orbital analysis of the Fermi surface in Fig. 1 we conclude that low values of the superconducting gaps are found on those regions of the Fermi surface with out-of-plane orbital character (S p_z and Nb d_{z^2}), while large values correspond to regions with in-plane character (Nb d_{xy} and $d_{x^2-y^2}$).

The regions of the Fermi surface with the largest superconducting gap coincide with the hot spots of the electronic EPI parameter $\lambda_{\mathbf{k}}^{\mathrm{el}}$, as shown in Fig. 5(c). In particular the EPI strength on the Γ-centered pockets exhibits a narrow distribution around $\lambda_{\mathbf{k}}^{\mathrm{el}} = 0.8$–$0.9$, while that on the K-centered pocket covers the wide range from $\lambda_{\mathbf{k}}^{\mathrm{el}} = 0.6$ to $\lambda_{\mathbf{k}}^{\mathrm{el}} = 3.0$. The resulting average EPI parameter is $\lambda^{\mathrm{el}} = 1.46$. We emphasize that, while $\lambda_{\mathbf{k},\nu}^{\mathrm{ph}}$ (Fig. 2) and $\lambda_{\mathbf{k}}^{\mathrm{el}}$ (Fig. 5) are related, they are not the same quantity. A detailed discussion of these quantities can be found in Ref. [55]. From this analysis it is clear that the two anharmonic modes contribute significantly to creating electron-phonon hot spots on the triangular arcs of the Fermi surface. While no charge ordering has been observed in 2H-NbS_2 thus far, our findings clearly indicate that the EPI with the anharmonic phonons places this system very close to a lattice instability [56]. This conclusion is further supported by the Fermi surface contribution to the adiabatic phonon self-energy [57] presented in Fig. S6 of the Supplemental Material [38]. Based on these considerations we propose that superconductivity in 2H-NbS_2 is driven by the same EPI that underlies a "latent" CDW instability, i.e., a CDW that is possibly quenched by quantum fluctuations.

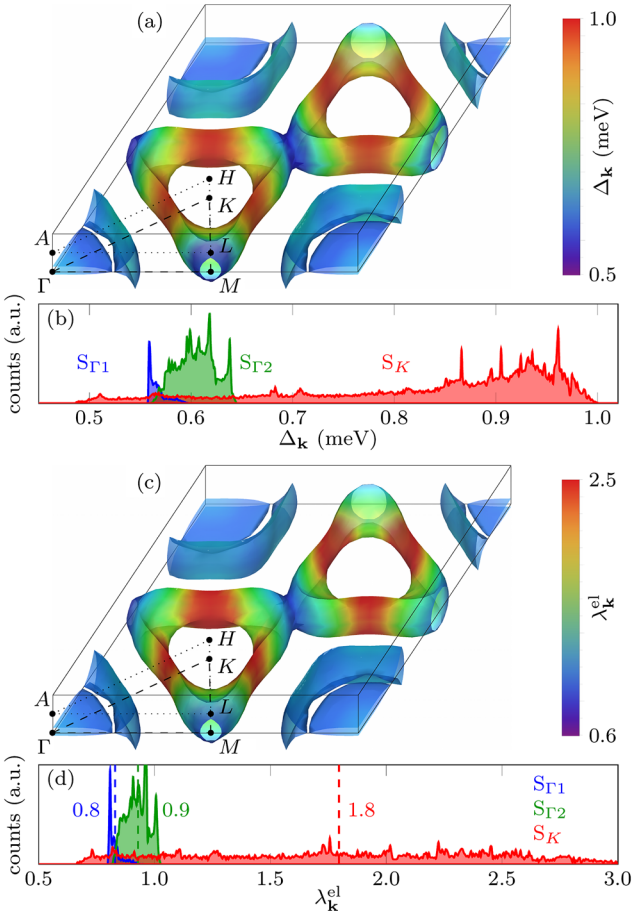

FIG. 5. (a) Momentum-resolved superconducting gap $\Delta_{\mathbf{k}}$ on the Fermi surface of 2H-NbS_2, calculated within the *ab initio* Migdal-Eliashberg theory for $T = 1.7$ K. (b) Energy distribution of the superconducting gap $\Delta_{\mathbf{k}}$, color coded by Fermi surface sheet: S_{Γ_1} (blue), S_{Γ_2} (green), and S_K (red). The values for the gaps were scaled as in Fig. 4. (c) Momentum-resolved EPI strength $\lambda_{\mathbf{k}}^{\mathrm{el}}$ on the Fermi surface of 2H-NbS_2. (d) Distribution of the EPI strength $\lambda_{\mathbf{k}}^{\mathrm{el}}$ by magnitude, color coded by Fermi surface sheet as in (b).

We now come back to the overestimation of the measured critical temperature in our calculations. At present it is unclear whether this overestimation relates to an inadequate description of anharmonic effects, to the use of the Migdal approximation, to the approximate treatment of retardation effects, or to the assumption of a constant DOS near the Fermi level in the Eliashberg theory [24]. In order to test the sensitivity of our results to some of these effects, we repeated our calculations (i) by varying the frequency of the anharmonic modes, and (ii) by varying the DOS via a rigid shift of the Fermi level. Figure S7 of the Supplemental Material [38] shows that our calculated T_c is insensitive to the frequency of the anharmonic modes over a wide range; therefore, we can exclude this scenario. In contrast, Fig. S8 of the Supplemental Material [38] shows that the critical temperature is in better agreement with experiments if we raise the Fermi level by only 200 meV. Motivated by this observation we performed quasiparticle GW calculations of the band structure of NbS_2 [26,27,55,58–60]. Figure S9 of the Supplemental Material [38] shows that GW quasiparticle corrections reduce the DOS at the Fermi energy by 18% with respect to our DFT calculations. By repeating our Eliashberg calculations with the corrected N_F and μ^* we find that the critical temperature also decreases by 18%. For completeness the superconducting gap calculated after including quasiparticle corrections is shown in Fig. S10 of the Supplemental Material [38]. Our most accurate value, $T_c = 15.3$ K, is in better agreement with experiment.

In conclusion, we used the anisotropic *ab initio* Migdal-Eliashberg theory including Coulomb interactions to elucidate the nature of the superconducting pairing in 2H-NbS_2. Our calculations indicate that a large contribution to the pairing comes from EPI hot spots on the triangular Fermi surface arcs, which signal a latent CDW instability. We successfully explained tunneling measurements in terms of two superconducting gaps, a large one associated with in-plane Nb orbitals, and a small one related to the out-of-plane orbitals of Nb and S. More generally, our work highlights the importance of determining accurate low-energy band structures and Fermi surfaces beyond DFT in order to achieve a fully *ab initio* description of the pairing mechanism in TMDs.

We gratefully acknowledge fruitful discussions with M. A. Perez Osorio, M. Zacharias, N. Zibouche, C. Verdi, and L. Boeri. This work was supported by Austrian Science Fund (FWF) Project No. J 3806-N36, the Leverhulme Trust (Grant No. RL-2012-001), the UK Engineering and Physical

Sciences Research Council (Grants No. EP/J009857/1 and No. EP/M020517/1), the European Union's Horizon 2020 program under Grant No. 696656 GrapheneCore1, the University of Oxford Advanced Research Computing (ARC) facility [61], and the ARCHER UK National Supercomputing Service under the "AMSEC" Leadership project.

*Present address: King's College London, Physics Department, Strand, London WC2R 2LS, United Kingdom.
†feliciano.giustino@materials.ox.ac.uk

[1] B. Sipos, A. F. Kusmartseva, A. Akrap, H. Berger, L. Forró, and E. Tutiš, Nat. Mater. **7**, 960 (2008).
[2] Q. H. Wang, K. Kalantar-Zadeh, A. Kis, J. N. Coleman, and M. S. Strano, Nat. Nanotechnol. **7**, 699 (2012).
[3] A. K. Geim and I. V. Grigorieva, Nature (London) **499**, 419 (2013).
[4] R. A. Klemm, Physica (Amsterdam) **514C**, 86 (2015).
[5] J. Wilson and A. Yoffe, Adv. Phys. **18**, 193 (1969).
[6] D. E. Moncton, J. D. Axe, and F. J. DiSalvo, Phys. Rev. Lett. **34**, 734 (1975).
[7] T. Valla, A. V. Fedorov, P. D. Johnson, P.-A. Glans, C. McGuinness, K. E. Smith, E. Y. Andrei, and H. Berger, Phys. Rev. Lett. **92**, 086401 (2004).
[8] F. Weber, S. Rosenkranz, J.-P. Castellan, R. Osborn, R. Hott, R. Heid, K.-P. Bohnen, T. Egami, A. H. Said, and D. Reznik, Phys. Rev. Lett. **107**, 107403 (2011).
[9] M. Calandra and F. Mauri, Phys. Rev. Lett. **106**, 196406 (2011).
[10] M. Rösner, S. Haas, and T. O. Wehling, Phys. Rev. B **90**, 245105 (2014).
[11] M. Leroux, I. Errea, M. Le Tacon, S.-M. Souliou, G. Garbarino, L. Cario, A. Bosak, F. Mauri, M. Calandra, and P. Rodière, Phys. Rev. B **92**, 140303 (2015).
[12] T. Das and K. Dolui, Phys. Rev. B **91**, 094510 (2015).
[13] M. Naito and S. Tanaka, J. Phys. Soc. Jpn. **51**, 219 (1982).
[14] I. Guillamón, H. Suderow, S. Vieira, L. Cario, P. Diener, and P. Rodière, Phys. Rev. Lett. **101**, 166407 (2008).
[15] Z.-L. Liu, L.-C. Cai, and X.-L. Zhang, J. Alloys Compd. **610**, 472 (2014).
[16] Y. Nishio, M. Shirai, N. Suzuki, and K. Motizuki, J. Phys. Soc. Jpn. **63**, 156 (1994).
[17] D. E. Moncton, J. D. Axe, and F. J. DiSalvo, Phys. Rev. B **16**, 801 (1977).
[18] M. Calandra, I. I. Mazin, and F. Mauri, Phys. Rev. B **80**, 241108 (2009).
[19] M. Leroux, M. Le Tacon, M. Calandra, L. Cario, M.-A. Méasson, P. Diener, E. Borrissenko, A. Bosak, and P. Rodière, Phys. Rev. B **86**, 155125 (2012).
[20] J. P. Perdew and A. Zunger, Phys. Rev. B **23**, 5048 (1981).
[21] D. M. Ceperley and B. J. Alder, Phys. Rev. Lett. **45**, 566 (1980).
[22] P. Giannozzi *et al.*, J. Phys. Condens. Matter **21**, 395502 (2009).
[23] F. Giustino, M. L. Cohen, and S. G. Louie, Phys. Rev. B **76**, 165108 (2007).
[24] E. R. Margine and F. Giustino, Phys. Rev. B **87**, 024505 (2013).
[25] S. Poncé, E. R. Margine, C. Verdi, and F. Giustino, Comput. Phys. Commun. **209**, 116 (2016).
[26] F. Giustino, M. L. Cohen, and S. G. Louie, Phys. Rev. B **81**, 115105 (2010).
[27] H. Lambert and F. Giustino, Phys. Rev. B **88**, 075117 (2013).
[28] A. A. Mostofi, J. R. Yates, Y.-S. Lee, I. Souza, D. Vanderbilt, and N. Marzari, Comput. Phys. Commun. **178**, 685 (2008).
[29] All calculations were performed for the optimized crystal structure ($a = 3.28$ Å, $c/a = 3.47$, and $z = 0.113$). The Nb atoms occupy the $2b$ Wyckoff sites $(0, 0, 1/4)$, and the S atoms the $4f$ sites $(1/3, 2/3, z)$. We used norm-conserving pseudopotentials [30] and a plane waves kinetic energy cutoff of 120 Ry. The electronic and vibrational Brillouin zones were sampled using $24 \times 24 \times 8$ and $6 \times 6 \times 2$ points, respectively. The screened Coulomb interaction was averaged over a $18 \times 18 \times 6$ Brillouin zone grid, and the Sternheimer equations were solved using $12 \times 12 \times 4$ grids. We used an energy cutoff for the dielectric matrix of 10 Ry. For the superconducting gap the EPW code was employed to interpolate all quantities onto $30 \times 30 \times 10$ grids, using 22 Wannier functions. The Matsubara frequency cutoff was set to 1 eV and the Dirac deltas were replaced by Lorentzians of width 25 meV (electrons) and 0.05 meV (phonons).
[30] S. Goedecker, M. Teter, and J. Hutter, Phys. Rev. B **54**, 1703 (1996).
[31] F. Jellinek, G. Brauer, and H. Müller, Nature (London) **185**, 376 (1960).
[32] P. B. Allen and B. Mitrović, in *Solid State Physics* (Academic Press, New York, 1982), Vol. 37.
[33] In our calculations, we chose ω_{el} to be the lowest plasma energy [34,35] and ω_{ph} the highest phonon energy of the system.
[34] P. Cudazzo, M. Gatti, and A. Rubio, Phys. Rev. B **86**, 075121 (2012).
[35] P. Cudazzo, E. Müller, C. Habenicht, M. Gatti, H. Berger, M. Knupfer, A. Rubio, and S. Huotari, New J. Phys. **18**, 103050 (2016).
[36] K.-H. Lee, K. J. Chang, and M. L. Cohen, Phys. Rev. B **52**, 1425 (1995).
[37] E. R. Margine, H. Lambert, and F. Giustino, Sci. Rep. **6**, 21414 (2016).
[38] See Supplemental Material at http://link.aps.org/supplemental/10.1103/PhysRevLett.119.087003 for Figs. S1–S10.
[39] M. Born, *Fest. Akad. D. Wiss. Göttingen: I. Math.- Phys. Klasse*, 1st ed. (Springer, Berlin, 1951).
[40] D. J. Hooton, Philos. Mag. **46**, 422 (1955).
[41] T. R. Koehler, Phys. Rev. Lett. **17**, 89 (1966).
[42] P. K. Lam and M. L. Cohen, Phys. Rev. B **25**, 6139 (1982).
[43] P. Souvatzis, O. Eriksson, M. I. Katsnelson, and S. P. Rudin, Phys. Rev. Lett. **100**, 095901 (2008).
[44] I. Errea, M. Calandra, and F. Mauri, Phys. Rev. Lett. **111**, 177002 (2013).
[45] F. Giustino, *Materials Modelling using Density Functional Theory: Properties and Predictions* (Oxford University Press, Oxford, 2014).
[46] W. Kohn, Phys. Rev. Lett. **2**, 393 (1959).
[47] M. I. Katsnelson, I. I. Naumov, and A. V. Trefilov, Phase Transitions **49**, 143 (1994).

[48] I. C. Bersuker, *The Jahn-Teller Effect*, 1st ed. (Cambridge University Press, Cambridge, England, 2006).
[49] C. Heil, H. Sormann, L. Boeri, M. Aichhorn, and W. von der Linden, Phys. Rev. B **90**, 115143 (2014).
[50] M. D. Johannes, I. I. Mazin, and C. A. Howells, Phys. Rev. B **73**, 205102 (2006).
[51] Calculations with frozen A_g phonon lead to similar results, as shown in Fig. S4 of the Supplemental Material [38].
[52] M. I. Katsnelson and A. V. Trefilov, JETP Lett. **42**, 485 (1985).
[53] J. Kačmarčík, Z. Pribulová, C. Marcenat, T. Klein, P. Rodière, L. Cario, and P. Samuely, Phys. Rev. B **82**, 014518 (2010).
[54] V. G. Tissen, M. R. Osorio, J. P. Brison, N. M. Nemes, M. García-Hernández, L. Cario, P. Rodière, S. Vieira, and H. Suderow, Phys. Rev. B **87**, 134502 (2013).
[55] F. Giustino, Rev. Mod. Phys. **89**, 015003 (2017).
[56] A. W. Overhauser, Phys. Rev. B **3**, 3173 (1971).
[57] P. Zhang, S. G. Louie, and M. L. Cohen, Phys. Rev. Lett. **94**, 225502 (2005).
[58] M. S. Hybertsen and S. G. Louie, Phys. Rev. B **34**, 5390 (1986).
[59] R. W. Godby and R. J. Needs, Phys. Rev. Lett. **62**, 1169 (1989).
[60] G. Onida, L. Reining, and A. Rubio, Rev. Mod. Phys. **74**, 601 (2002).
[61] http://dx.doi.org/810.5281/zenodo.22558.